Diffraction of weakly unstable detonation through an obstacle with different sizes and shapes

Yuan Wang [1,*] Zheng Chen,[2] and Haitao Chen[1,†]
[1]*Institute of Applied Physics and Computational Mathematics, Beijing 100094, China*
[2]*SKLTCS, CAPT, BIC-ESAT, College of Engineering, Peking University, Beijing 100871, China*

(Received 26 October 2020; accepted 9 April 2021; published 29 April 2021)

Detonation diffraction has been extensively studied because it is a very fundamental problem and has broad practical applications. In this study, two-dimensional simulations considering detailed chemistry and transport are conducted to investigate the weakly unstable detonation diffracting through an obstacle. The emphasis is placed on assessing the effects of obstacle size and shape on detonation diffraction. For a semicircular obstacle, the subcritical, critical, and supercritical regimes are identified by increasing the obstacle radius. The competition between the energy release rate and expansion rate is analyzed; it interprets the regime distribution. Increasing the radius of a semicircular obstacle can reduce the curvature and thereby the expansion rate. The energy release rate dominates over the loss due to expansion during the diffraction process with a large obstacle radius. For triangular and rectangular obstacles, the supercritical regime without detonation quenching is not observed in the present simulations. Furthermore, the critical regime for transverse detonation formation is investigated and the critical obstacle sizes are compared for different obstacle geometries. It is found that the semicircular obstacle has the smallest critical size while the rectangular obstacle has the largest critical size. Unlike the critical obstacle size, the wall reflection distance of transverse detonation is independent of the obstacle geometry and it varies in the range of 10–15 times the detonation cell width. The characteristics of transverse detonation are compared for two weakly unstable mixtures, hydrogen/air without and with nitrogen dilution. A pair of transverse detonations induced by local explosion is observed in hydrogen/air with nitrogen dilution, which is quite different from the single transverse detonation in hydrogen/air. The comparison of the three regimes' distributions for these two mixtures shows that a larger obstacle size is required for transverse detonation formation in hydrogen/air with nitrogen dilution. However, the critical obstacle size normalized by the corresponding detonation induction length becomes closer for two mixtures. This indicates that the formation of transverse detonation is nearly independent of nitrogen dilution for weakly unstable mixtures.

DOI: 10.1103/PhysRevFluids.6.043201

I. INTRODUCTION

It is well known that when a detonation propagates in a channel with an obstacle, the diffraction phenomenon occurs due to the increased cross-sectional area [1–3]. Affected by the expansion wave emanating at the expansion corner, the reaction front may decouple with the leading shock and detonation quenching may occur during the diffraction process. Thereafter, the new transverse

*wy91@pku.edu.cn
†chen_haitao@iapcm.ac.cn

detonation forms under certain conditions and sweeps along the diffracted wave front, resulting in the detonation reinitiation [4,5].

Detonation diffraction has drawn much attention because it is a fundamental problem for research of detonation quenching and reinitiation mechanisms. In practical applications such as pulse detonation engines (PDEs), as the detonation propagates from the pre-detonator to the main detonable domain, the diffraction phenomenon might occur and the detonation failure or reinitiation determined by geometrical dimension is crucial for the design of the initiators. Therefore, in the past few decades, many studies have been conducted to understand the detonation diffraction phenomenon. In the literature, generally, the diffraction process is classified as subcritical and supercritical regimes based on the detonation failure or successful reinitiation [5–9]. In the subcritical regime, the shock wave is partially decoupled from the reaction front and detonation fails. However, in the supercritical regime, the transverse detonation forms and sweeps along the diffracted wave, resulting in shock-reaction front recoupling and thereby successful detonation reinitiation. The experimental studies by Kawasaki and Kasahara [9] and numerical simulations by Gallier *et al.* [7] both investigated the detonation diffraction during its propagation from a channel into an unconfined space. The wall reflection distance of transverse detonation was found to be in the range of 10–15 times the detonation cell width. Similar phenomena were also observed by Nagura *et al.* [10,11]. Bartlmä and Schröder [6] conducted a series of experiments on detonation diffracting at a convex corner with different wall angles. They found that the regime distributions are affect by the wall angle during the detonation diffraction process, and that the transverse detonation forms only if the wall angle exceeds 45°. They also found that the shape of diffracted shock has self-similarity and thereby it can be described by the Chester-Chisnell- Whitham theory [12].

Recently, Yuan *et al.* [5] has proposed a semianalytical model to predict the trajectory of transverse detonation in the supercritical regime with successful detonation reinitiation. Different from the above regime classification during the detonation diffraction process, Pintgen and Shepherd [13] defined the critical regime dividing it into subcritical and supercritical outcomes without and with the formation of transverse detonation, respectively. According to the position of transverse detonation formation, Edwards *et al.* [2] defined the supercritical case with transverse detonation appearing along the wedge while the transverse detonation forms at the apex of the wedge for the critical case. Soloukhin and Ragland [14] and Arienti and Shepherd [15] defined three detonation diffraction regimes: the supercritical regime with a continuous transition of the detonation, the critical regime with a partial shock-reaction front decoupling and subsequent detonation reinitiation induced by the formation of transverse detonation, and the subcritical regime with complete shock-reaction front decoupling without reinitiation. The transition among these three regimes was achieved through changing the initial pressure or the activation energy. Murray and Lee [4,16] proposed that the energy release rate and expansion rate behind the diffracted shock wave determine the detonation diffraction regime. For the subcritical regime the expansion rate exceeds the energy release rate, while for the supercritical regime the energy release rate dominates. Besides, they revealed two reinitiation mechanisms. The first one is that local explosion induces successful reinitiation, and the second one is that the reflection of the diffracted wave from the wall results in successful reinitiation. Schultz [17] developed a critical diffraction model to separate the subcritical and supercritical regimes through initial conditions, which was validated by his experiments.

Most of the above-mentioned studies focused on the determination of detonation diffraction regimes. Generally, the mixture composition, initial pressure, and tube or channel geometry were considered. However, the influence of obstacle geometry (including its size and shape) on detonation diffraction received little attention. Besides, previous studies mainly investigated the detonation diffraction behind an obstacle or through an abrupt change in area with constant wall angle. Detonation diffraction caused by an obstacle with a varying wall angle, such as a circular obstacle, is not well known. Based on the above discussion, here we consider two-dimensional (2D) detonation diffraction through an obstacle. Weakly unstable hydrogen/oxygen with different nitrogen dilution are used. Detailed chemistry and diffusive transport are accurately considered in the simulations.

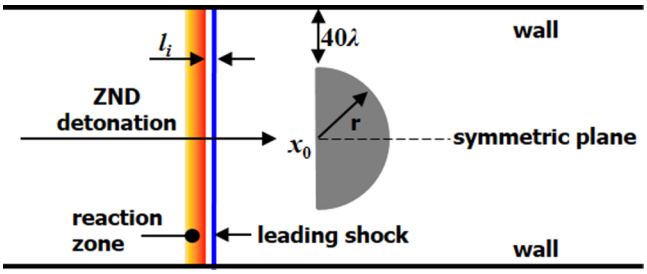

FIG. 1. Schematic of detonation diffracting through a semicircular obstacle.

The objective is to examine the effects of obstacle size and shape on detonation diffraction. The detonation quenching, reinitiation, and transverse detonation formation are investigated.

II. NUMERICAL MODEL AND METHODS

We consider 2D detonation diffracting through an obstacle. As sketched in Fig. 1, the Zel'dovich von-Neumann Döring (ZND) detonation consisting of the leading shock and reaction zone, with the induction length of l_i, is used as the initial condition and it propagates to the unburned mixture on the right side. To assess the obstacle geometry on detonation diffraction, we consider an obstacle with different shapes (semicircular, triangular, and rectangular) and different sizes.

The unburned mixture is stoichiometric $H_2/O_2/N_2$ with a molar ratio of $H_2 : O_2 : N_2 = 2 : 1 : s$. We consider two values of nitrogen dilution, $s = 3.76$ and 7, with the former corresponding to the stoichiometric H_2/air. Table I shows the induction length, l_i, and detonation cell size, λ, for these two mixtures. The unburned mixtures are initially at $T_0 = 300$ K and $P_0 = 1$ atm. Due to the symmetry, only half of the computational domain in Fig. 1 is considered and the symmetric boundary condition is used at the symmetric plane. The adiabatic, no-slip wall boundary conditions are used on the top wall and on the obstacle surfaces. The reflective boundary condition is used on the obstacle surface. The simulations considering both wall and reflective boundary conditions on obstacle surface, respectively, were conducted and results indicated that the wall boundary layer slightly affects the shape of the transverse wave. However, the regime distributions of detonation diffraction are the same for simulations considering both wall and reflective boundary conditions on an obstacle surface, respectively (see Fig. 23 in Appendix D). To ensure the successful detonation diffraction through the obstacle with various cross-sectional areas, the vertical distance between the wall and upper corner of obstacle is set to 40λ, which is much larger than the critical channel width of 10λ for successful detonation propagation [1].

The parallel block structured mesh refinement framework AMROC [18] is used to simulate 2D detonation diffracting. The conservation equations for unsteady, compressible, multicomponent, reactive flow are solved in AMROC using the finite volume method. Diffusion terms are kept in the conservation equations. The CHEMKIN packages are utilized to evaluate the thermotransport properties and reaction rates. A hybrid Roe-HLL Riemann solver for mixtures of thermally perfect gases was used to calculate the convective fluxes. A second-order accurate central difference scheme was used for multispecies diffusion terms. The semi-implicit Runge-Kutta method GRK4A was adopted

TABLE I. Initial conditions and detonation properties of two mixtures considered in this study.

Mixture	T_0 (K)	P_0 (atm)	$H_2 : O_2 : N_2$	l_i (mm)	λ (mm)
Mixture 1	300	1	2:1:3.76	0.19	0.61
Mixture 2	300	1	2:1:7	1.254	3.85

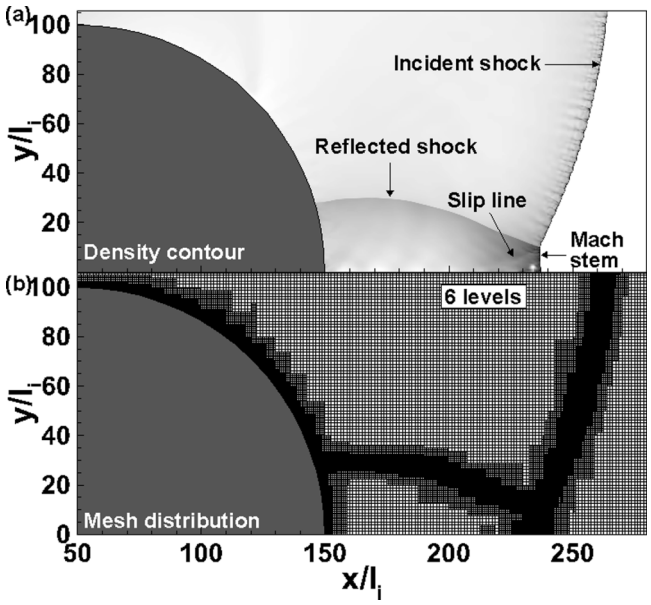

FIG. 2. (a) Density contour and (b) distribution of six mesh levels for detonation propagating through a semicircular obstacle and corresponding formation of Mach reflection.

to integrate stiff reaction terms. The Godunov splitting method was used to decouple hydrodynamic transport and stiff chemical reaction source numerically. The target CFL number of 0.98 was used together with a dynamic time step adjustment. The hydrogen chemistry developed by Li *et al.* [19] is considered. AMROC has been successfully used in previous studies on detonation initiation and propagation (e.g., [20–24]). The details on governing equations and numerical schemes of AMROC can be found in Ref. [18] and thereby are not repeated here. Moreover, the simulations for detonation diffracting through an obstacle with and without diffusion terms were conducted and the results indicate that the influence of diffusion terms on detonation diffraction is negligible (see Fig. 22 in Appendix C).

To accurately and efficiently resolve the detonation diffraction process, dynamically adaptive mesh refinement is used in simulations. Mesh refinement or coarsening is determined by the local temperature, pressure, and density gradients. Figure 2 shows the density contour for detonation diffracting through a semicircular obstacle and corresponding mesh distributions. The base mesh size is $250 \times 250\,\mu\text{m}^2$. After six level mesh refinements, the finest mesh size is $3.9 \times 3.9\,\mu\text{m}^2$. Since the detonation induction length is $l_i = 0.19$ mm and 1.254 mm for mixtures 1 and 2, respectively, there are more than 45 grid points covering the induction zone. Moreover, the region close to the obstacle surface is always covered by the finest mesh as shown in Fig. 2(b). This ensures that the detonation diffraction process is adequately resolved. In addition, the simulations with different base mesh sizes and mesh levels are conducted to ensure grid convergence. The results are shown in Appendix B.

To validate the present numerical model and simulation setup, we compare our simulation results with those from the experiments reported in Ref. [13]. Specifically, detonation propagating from a tube into an unconfined half-space in hydrogen/oxygen/argon (with a molar ratio of $H_2 : O_2 : Ar = 0.22 : 0.11 : 0.67$) at 100 kPa and 295 K is considered. Figure 3 shows the critical cases with the generation of a transverse wave developed from local explosion. Good agreement between the present computational and experimental results was observed, except the discrepancies of detonation front distance and shape caused by the different positions of local explosion.

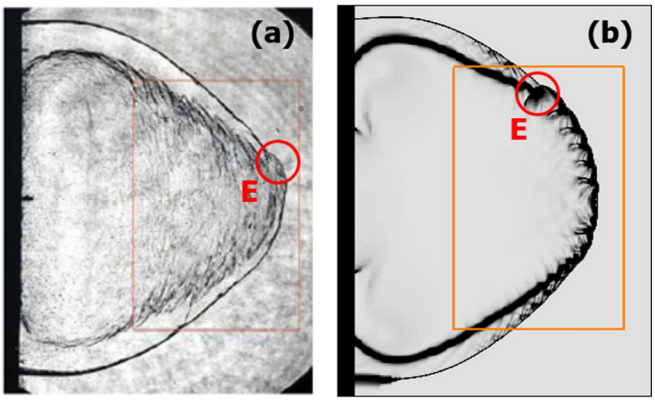

FIG. 3. Schlieren contour for $0.22\ H_2 + 0.11\ O_2 + 0.67$ Ar at $P_0 = 100$ kPa and $T_0 = 295$ K. (a) experimental result from [13] and (b) present simulation result. Red circles represent the positions of local explosion, E.

III. RESULTS AND DISCUSSION

A. Detonation diffracting through a semicircular obstacle

First we consider detonation diffracting through a semicircular obstacle in stoichiometric H_2/air (mixture 1). Different obstacle sizes are considered to assess their effects on detonation diffraction, especially on quenching and reinitiation of detonation. Different from previous studies [25,26] on detonation propagation through a circular obstacle, this study considers a semicircular obstacle so that the effects of Mach reflection of detonation on the left semicircular obstacle with decreasing cross-sectional area are eliminated. In addition, according to the experiments by Moen *et al.* [27] who studied detonation diffraction through a tube and orifice plate, the detonation diffraction is mainly determined by the local wave front. Therefore, at the beginning of the detonation collision with the obstacle, the abrupt change in area has little influence on the subsequent detonation diffraction, especially on the regimes' distributions of detonation diffraction.

In Table II, three regimes of detonation diffraction through a semicircular obstacle are identified based on the criteria of whether or not the leading shock decouples with the reaction front and the reinitiation is achieved: (1) the subcritical regime with shock-reaction front decoupling, (2) the critical regime with shock-reaction front decoupling and subsequent detonation reinitiation, and (3) the supercritical regime without shock-reaction front decoupling. Figure 4 schematically illustrates the above three regimes. For the subcritical regime with $r/l_i = 12.5$ in Fig. 4(a), the reaction front (red lines) starts to decouple with the leading shock (blue lines) as the detonation propagates along the obstacle and there is no recoupling between the reaction front and leading shock until the leading shocks collide with each other at the symmetric plane. For the critical regime with $r/l_i = 50$ in Fig. 4(b), the decoupling and then recoupling between the reaction front and leading shock occur before the leading shocks collide at the symmetric plane. For the supercritical regime with $r/l_i = 100$ in Fig. 4(c), the reaction front always couples with the leading shock during the detonation diffracting through the semicircular obstacle.

TABLE II. Distributions of three regimes with different radii of a semicircular obstacle.

Normalized obstacle radius, r/l_i	12.5	50	100
Regimes	Subcritical	Critical	Supercritical

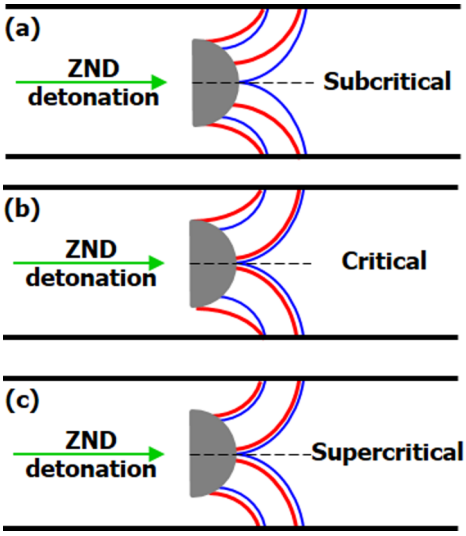

FIG. 4. Schematic of three regimes: (a) subcritical regime, (b) critical regime, and (c) supercritical regime during detonation diffracting through a semicircular obstacle (in gray). The blue lines represent the shock wave and the red lines denote the reaction zone.

Figure 5 shows the evolution of temperature contours for the subcritical case of $r/l_i = 12.5$. At $t = 4.9\,\mu$s, the planar detonation propagates toward the obstacle at the Chapman Jouget (CJ) speed of 1975 m/s. Around $t = 5.7\,\mu$s, the detonation collides with the obstacle and a curved shock near the obstacle surface is formed. The reaction front decouples with the leading shock until the diffracted angle θ, defined as the angle between the tangent line of an obstacle surface and a horizontal line, is larger than 30° at $t = 6.2\,\mu$s. This is consistent with the results of [5], in which the detonation wave can propagate sustainably without shock-reaction front decoupling if the diffracted angle is less than 30°. This is because the expansion of the detonation wave is sufficiently small at the relatively small diffracted angle. As the detonation propagates forward with the increased diffracted

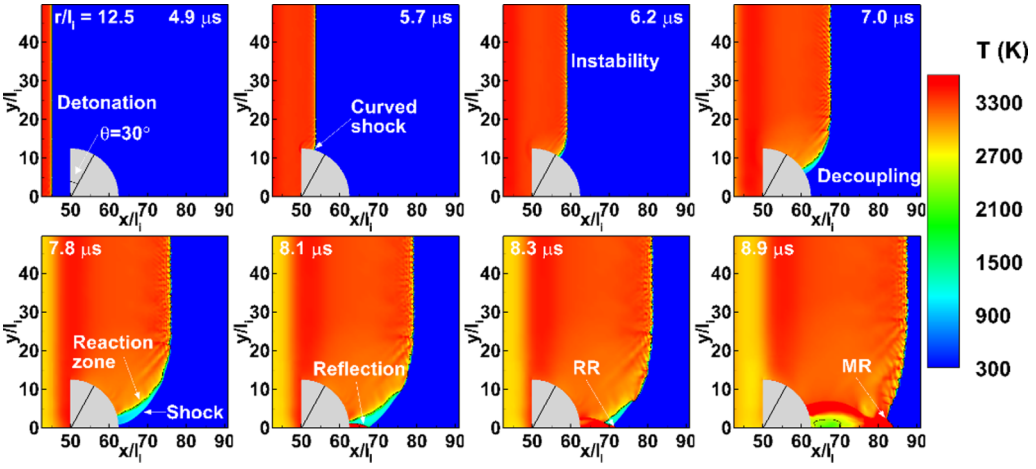

FIG. 5. Evolution of temperature contours during detonation diffracting through a semicircular obstacle with $r/l_i = 12.5$. RR: regular reflection; MR: Mach reflection. The black isolines correspond to temperature equal to 2400 K.

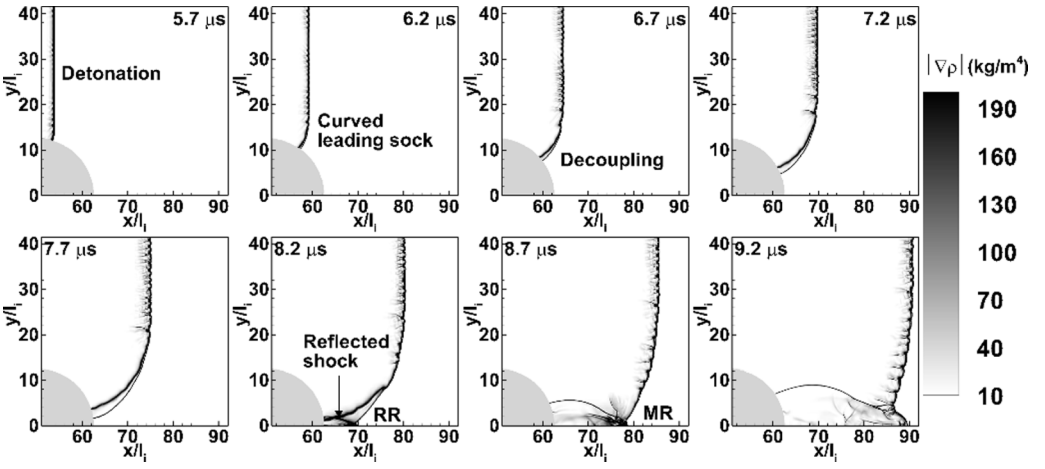

FIG. 6. Evolution of density gradient contours during detonation diffracting through a semicircular obstacle with $r/l_i = 12.5$. RR: regular reflection; MR: Mach reflection.

angle, the distance between the reaction front and leading shock further increases and the region of unreacted mixture compressed by leading shock extends during $6.2 < t < 7.8\,\mu$s. At $t = 8.1\,\mu$s, the leading shock reflects at the symmetric plane and the reflected shock sweeps along the shocked but unreacted mixtures. At $t = 8.9\,\mu$s, the Mach reflection transformed from regular reflection is observed. As the detonation propagates along the semicircular obstacle surface, an expansion wave originating from the obstacle corner weakens and decelerates the strength of the detonation wave near the obstacle surface. Hence, the reaction front decouples with the leading shock and detonation fails and its cellular structure disappears [6,15].

Figure 6 shows the density gradient distributions at different times for a semicircular obstacle with $r/l_i = 12.5$. Again, the shock-reaction front decoupling is observed from $t = 6.2\,\mu$s to $t = 7.7\,\mu$s and the corresponding vertical height increases from $y/l_i = 14$ to $y/l_i = 21$. When the leading shock reflects at $t = 8.2\,\mu$s, the region of shock-reaction front decoupling significantly decreases to $y/l_i = 8$ caused by the termination of the detonation diffraction process. However, the transverse detonation (details on transverse detonation will be discussed later) cannot form due to the small obstacle radius with limited detonation diffraction duration. At $t = 8.7\,\mu$s, the reflected shock sweeps along the shocked but unreacted mixtures and brings them to react completely. The Mach reflection is observed at $t = 9.2\,\mu$s and it consists of an incident detonation wave, an overdriven reactive Mach stem, and a reflected shock intersecting at the triple point. A similar phenomenon was reported by Li *et al.* [28].

When the obstacle radius is increased to $r/l_i = 50$, a similar phenomenon is also observed in Fig. 7 before $t = 11\,\mu$s. However, the transverse detonation induced by a local explosion forms around $t = 12.5\,\mu$s and it propagates backward and sweeps along the shocked but unreacted mixtures [2,5,13]. At $t = 13.4\,\mu$s, the transverse detonation collides with the obstacle surface and successful detonation reinitiation is achieved. Note that the transverse detonation forms only if the diffracted angle exceeds a value of about 45°. These results agree with the experimental observation of Bartlmä and Schröder [6], in which the plane with various wall angles was inserted to test the detonation diffraction. As the detonation propagates forward, the leading shocks collide and reflect at the symmetric plane and Mach reflection is observed. Different from the results for small obstacle radius of $r/l_i = 12.5$, increasing the obstacle radius to $r/l_i = 50$ results in the decrease of curvature of the semicircular obstacle. The relatively small expansion rate at smaller curvature of the obstacle is able to shorten the region of shocked but unreacted mixtures (see Fig. 7 at $t = 11\,\mu$s). Besides, as the obstacle radius increases, there is a longer time for the development of a local explosion

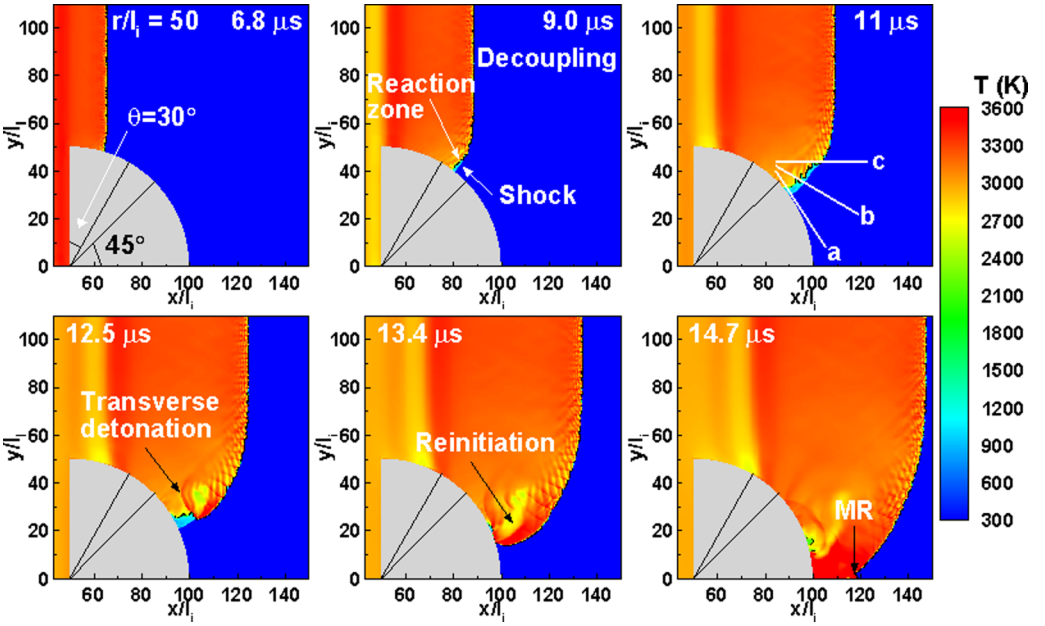

FIG. 7. Evolution of temperature contours during detonation diffracting through a semicircular obstacle with $r/l_i = 50$. MR: Mach reflection. The black isolines correspond to temperature equal to 2400 K.

and subsequent transverse detonation. Therefore, the critical regime with the successful detonation reinitiation is achieved for a middle obstacle radius of $r/l_i = 50$.

To describe the detonation diffraction and formation of transverse detonation, the density gradient distributions at different times are plotted in Fig. 8. Before the formation of transverse detonation, the region of shock-reaction front decoupling increases from $t = 9\ \mu$s (line 3) to $t = 10.5\ \mu$s

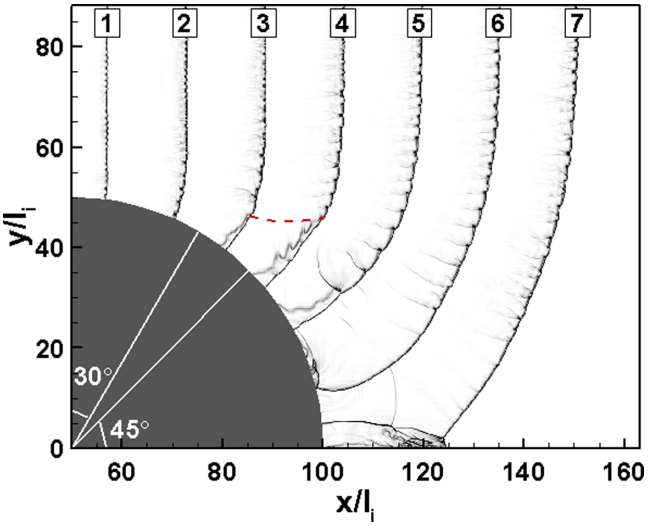

FIG. 8. Density gradient distributions during detonation diffracting through a semicircular obstacle with $r/l_i = 50$. The time sequence for lines 1–7 is 1: 6 μs; 2: 7.5 μs; 3: 9 μs; 4: 10.5 μs; 5: 12 μs; 6: 13.5 μs; 7: 15 μs.

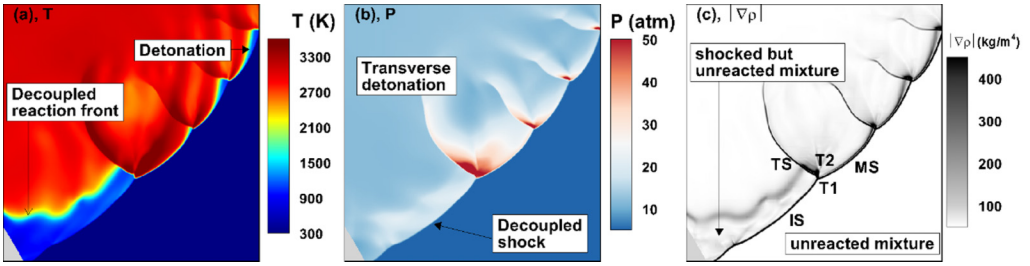

FIG. 9. Enlarged temperature, pressure, and density gradient contours at $t = 12\ \mu$s for detonation diffracting through a semicircular obstacle with $r/l_i = 50$.

(line 4). Besides, different from the results shown in Figs. 5 and 6, the reaction front becomes wrinkled at $t = 10.5\ \mu$s for $r/l_i = 50$. This is mainly due to the generation of Richtmyer-Meshkov (RM) instabilities induced by the folded shock propagating across the shocked but unreacted mixture with density gradient. At $t = 12\ \mu$s (line 5), the interactions of expansion waves and leading shock lead to a local pressure maximum, which results in a fold in the shock front. The folded shock induces the local explosion and formation of transverse detonation, which propagates backward and collides with the obstacle at $t = 13.5\ \mu$s (line 6). At $t = 15\ \mu$s (line 7), the Mach reflection forms around the symmetric plane.

To visualize the details on transverse detonation structure, we plot the enlarged temperature, pressure, and density gradient contours of the transverse detonation in Fig. 9. The transverse detonation was found in many previous studies [3,5–8,10,11,13,15,29]. As the detonation diffracts along the obstacle surface, the shock fronts start to fold and collide, which induces the generation of transverse detonation on the expansion wave front [2,15]. The transverse detonation is highly overdriven [6]. The higher temperature and pressure behind the transverse wave front are observed in Figs. 9(a) and 9(b), respectively. The transverse detonation propagates toward the obstacle surface and sweeps along the front of shocked but unreacted mixtures in the blue region in Fig. 9(a). The detonation reinitiation is achieved up to the reflection of the transverse detonation at the obstacle surface [8]. Figure 9(c) shows that the transverse detonation consists of the incident shock (denoted as IS), Mach stem (denoted as MS), and transverse shock (denoted as TS) [15]. The incident shock with lower shock strength is nonreactive, while the Mach stem with higher shock strength results in the shorter distance between the shock and reaction front. The transverse wave originated from two triple points T1 and T2, which propagates along the region of shocked but unreacted mixture. This mixture is completely burned after being passed by the transverse wave (see Fig. 7 at 13.4 μs).

To further demonstrate the processes of transverse detonation sweeping along the incident shock, the temperature and pressure distributions along lines *a*–*c* of Fig. 7 are shown in Figs. 10(a)–10(c), respectively. The gray zones correspond to the shock-reaction front decoupling. Along line *a*, the shock-reaction front decoupling is observed once the diffracted angle exceeds 30°. At $t = 9\ \mu$s, the normalized pressure of leading shock attenuates to $P/P_0 = 11.4$, which is much smaller than the corresponding value at the von Neumann state of $P_{\rm vN}/P_0 = 27$. As the detonation propagates forward, the distance between the shock and reaction front continually increases from $x/l_i = 1.1$ for line 1 at $t = 9\ \mu$s to $x/l_i = 2.2$ for line 4 at $t = 12.4\ \mu$s [see temperature distribution in Fig. 10(a)]. Along lines *b* and *c*, the shock-reaction front decoupling appears at $t = 9$ and 10.3 μs, respectively. The above phenomenon indicates that the shock-reaction front decoupling first occurs near the obstacle surface and then extends along the incident shock. On the contrary, the transverse detonation first appears along line *c* at $t = 11.6\ \mu$s and propagates backward and reflects at the obstacle surface around $t = 13.4\ \mu$s (see Fig. 7).

With further increasing of the obstacle radius to $r/l_i = 100$, the distinctive behaviors can be identified in Fig. 11. There is no shock-reaction front decoupling as the detonation diffracts along

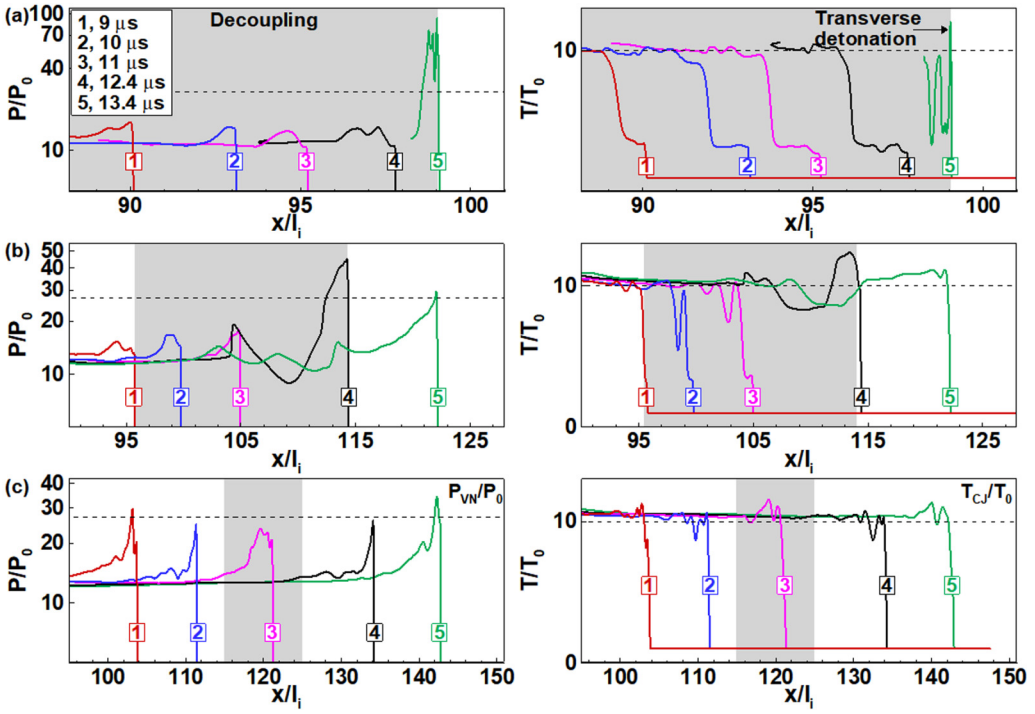

FIG. 10. Change of normalized pressure, P/P_0, and temperature, T/T_0, after the leading shock with normalized shock position, x/l_i, along the lines a–c in Fig. 7 for a semicircular obstacle with $r/l_i = 50$. The gray zones correspond to the shock-reaction front decoupling.

the obstacle surface. When the leading shocks collide at the symmetric plane, the strong reflected shocks are produced and consequently the regular and Mach reflections develop.

In previous studies [3,5,6,13,15], the diffracted angle, e.g., the wall angle, was usually fixed. However, for the semicircular obstacle considered here, the detonation propagates along the obstacle with increased diffracted angle. Once the diffracted angle exceeds 30°, the reaction front starts to decouple with the leading shock. Figure 12(a) shows that for $r/l_i = 100$ and $\theta = 34°$, several

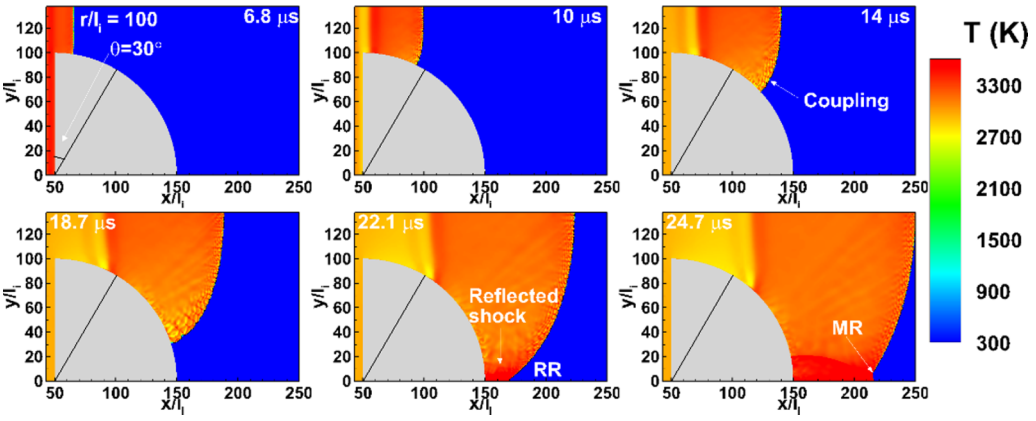

FIG. 11. Evolution of temperature contours for a semicircular obstacle with $r/l_i = 100$. RR: regular reflection; MR: Mach reflection.

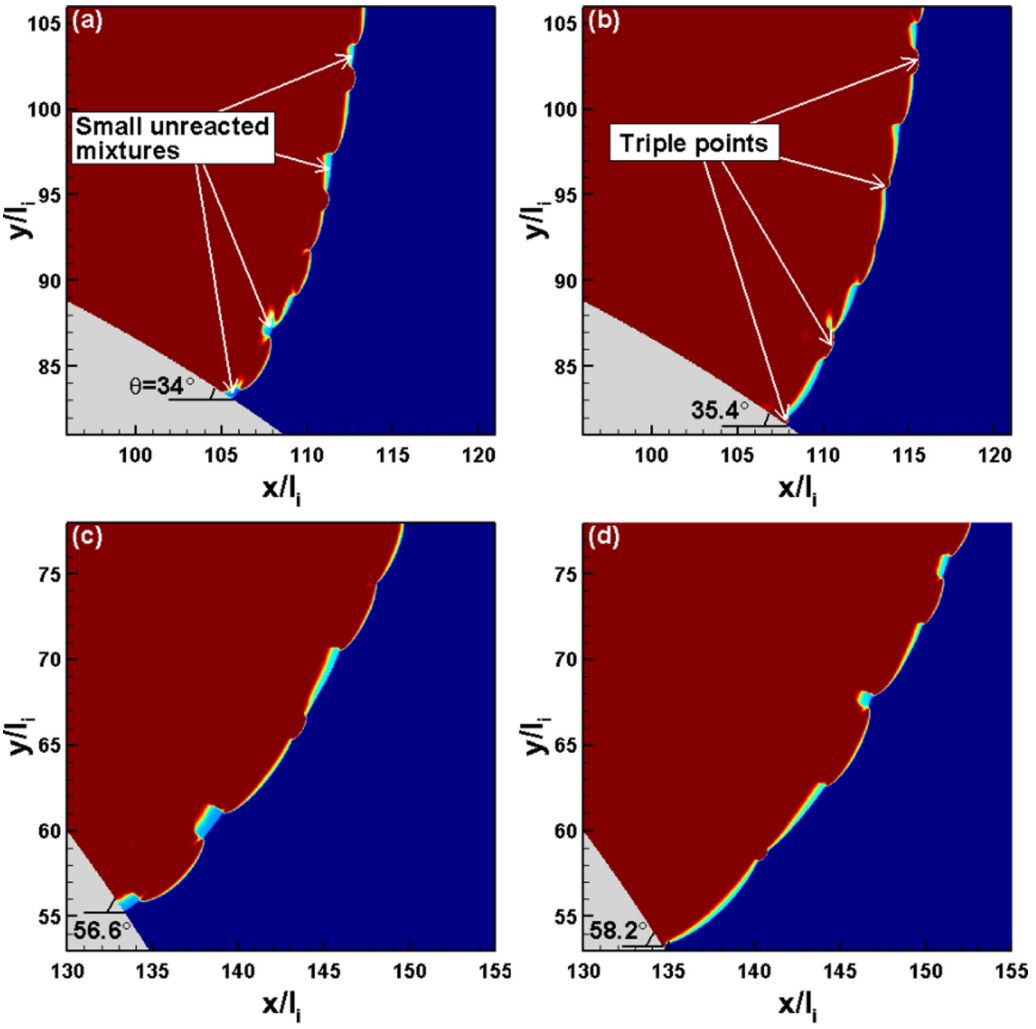

FIG. 12. Enlarged temperature contours for a semicircular obstacle with $r/l_i = 100$.

separated regions with shocked but unreacted mixtures distribute along the curved detonation wave front, which is different from the continuous distribution of the shocked but unreacted mixtures as shown in Figs. 5 and 7 for relatively smaller obstacle radius. In Fig. 12(b) for $\theta = 35.4°$, the detonation further propagates forward and the triple points merge with the shocked but unreacted mixtures. The same processes occur repeatedly in the next two frames in Fig. 12 for larger diffracted angles. Note that the curvature of a semicircular obstacle is further decreased for $r/l_i = 100$, resulting in the smaller expansion rate and thereby the energy release rate controlled by chemical reactions dominates the detonation diffraction process. Therefore, the diffraction along an obstacle without detonation quenching is identified as the supercritical regime.

Figure 13 shows the density gradient distribution for a semicircular obstacle with $r/l_i = 100$. There is no shock-reaction front decoupling, and only the spacing of transverse waves near the obstacle surface increases. The triple points always exist during the diffraction process.

Figure 14 shows the change of leading shock pressure near the obstacle surface with its horizontal position for different obstacle radii of $r/l_i = 12.5$, 50, and 100. Along the obstacle, the pressure of leading shock obviously attenuates for $r/l_i = 12.5$ and 50, which is caused by the shock-reaction

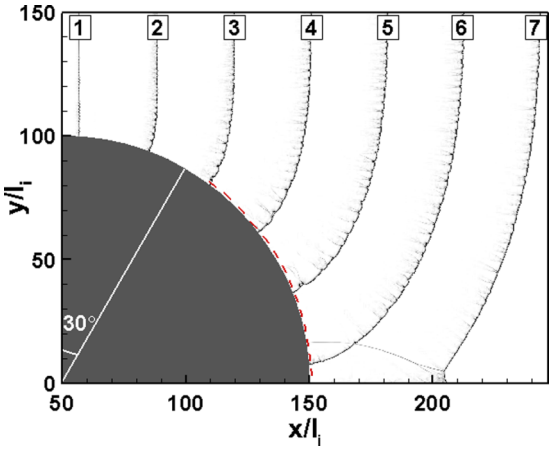

FIG. 13. Density gradient distributions for a semicircular obstacle with $r/l_i = 100$ at different simulation times.

front decoupling. However, for $r/l_i = 100$ a much smaller decrease in leading shock pressure is observed and thereby there is no shock-reaction front decoupling. A local explosion and subsequent formation of transverse detonation for $r/l_i = 50$ is induced by the interactions of folded shock waves, which results in an abrupt pressure rise to $P/P_{vN} = 3.2$. After passing the obstacle, the leading shocks collide and reflect at the symmetric plane for these three obstacle radii, resulting in a peak pressure close to five times the von Neumann value. Then the peak pressure gradually decays as it propagates forward.

The above results are for detonation diffraction process initialized by ZND detonation. It is noted that the cellular instability might affect the detonation diffraction process when a fully developed cellular detonation was considered. Therefore, the simulations for detonation diffracting through an obstacle with cellular detonation initiation were performed and the comparisons between results for ZND and cellular detonation initiation were investigated. The results (see Fig. 20 in

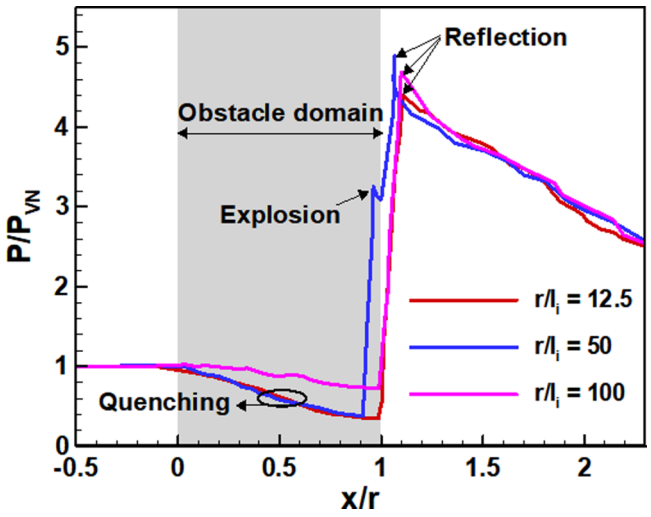

FIG. 14. Normalized pressure of leading shock, P/P_{vN}, near the obstacle surface with its normalized horizontal position, x/r, for a semicircular obstacle with different obstacle radii.

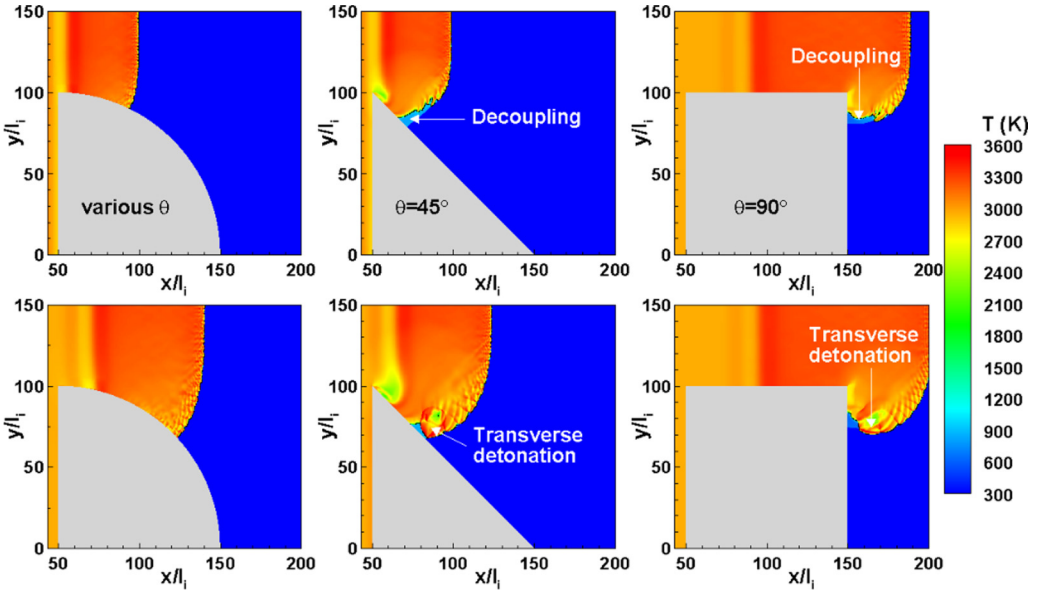

FIG. 15. Evolution of temperature contours for $r/l_i = 100$ with different obstacle shapes.

Appendix A) show that the critical obstacle radius of transverse detonation formation for cellular detonation initiation is smaller than that for ZND detonation. This indicates that the cellular instability can promote the reinitiation process in a stoichiometric H_2/air mixture. The cellular instabilities result in the interaction of the transverse shock waves [30,31]. The collisions between the transverse shock waves induce local explosions and follow the formation of transverse detonation, which indicates the detonation reinitiation.

B. Effects of obstacle shape and mixture composition

In previous studies, a channel or tube with an obstacle of $\theta = 90^\circ$ is usually used to investigate the detonation diffraction and the supercritical regime is defined when the transverse detonation forms [14,15]. Here we also consider the detonation diffraction through triangular ($\theta = 45^\circ$) and rectangular obstacles ($\theta = 90^\circ$). The results compared with those for a semicircular obstacle are shown in Fig. 15. The size of these three obstacles is fixed to $r/l_i = 100$ (r represents length for triangular and rectangular obstacles). As discussed in the above subsection, the supercritical regime without successive shock-reaction front decoupling is observed for the semicircular obstacle (also shown in Figs. 11–13). For triangular and rectangular obstacles, however, the shock-reaction front decouples first and then detonation reinitiation is induced by the transverse detonation. Therefore, the detonation diffraction through triangular and rectangular obstacles is in the critical regime.

The results for triangular and rectangular obstacles are similar to that for semicircular obstacle for $r/l_i = 12.5$ and 50 and thus are not shown here. In Table III we summarize the distributions of three regimes based on obstacle size and shape. The supercritical regime appears only for a semicircular obstacle with a large size of $r/l_i = 100$ and 200. Besides the obstacle size, the obstacle shape can greatly affect the regime distributions. For example, the critical obstacle size for critical regime with formation of transverse detonation is $r/l_i = 25$ and 50 for the semicircular and the rectangular obstacle, respectively. This indicates that longer time and distance are required to form transverse detonation for the rectangular obstacle.

The formation of transverse detonation is crucial during the detonation diffraction process. The original position, wall reflection point, and the trajectory of transverse detonation were studied

TABLE III. Distributions of three regimes with different obstacle sizes and shapes.

Normalized obstacle size, r/l_i	Semicircular obstacle	Triangular obstacle	Rectangular obstacle
12.5	Subcritical	Subcritical	Subcritical
25	Critical	Subcritical	Subcritical
37.5	Critical	Critical	Subcritical
50	Critical	Critical	Critical
100	Supercritical	Critical	Critical
200	Supercritical	Critical	Critical

before. Among them, the wall reflection distance from the position of the obstacle apex or channel or tube end corner to the reflection point of the transverse detonation is an important variable [5,7,10,11]. In Fig. 16 we plot the change of the wall reflection distance normalized by cell size, l_w/λ, with the obstacle size normalized by detonation induction length, r/l_i. The results for different obstacle shapes are plotted together for comparison. The gray zone represents the subcritical regime with wall reflection distance less than the obstacle size. Figure 16 shows that the wall reflection distance is in the range of 10–15 times the cell width and it is nearly independent of both the obstacle size and shape. This is consistent with the results obtained by Nagura *et al.* [10].

The above results are for mixture 1 with $H_2 : O_2 : N_2 = 2 : 1 : 3.76$. We also consider nitrogen-diluted mixture 2 with $H_2 : O_2 : N_2 = 2 : 1 : 7$. As mentioned in Sec. II, the induction length increases from $l_i = 0.19$ mm for mixture 1 to $l_i = 1.254$ mm for mixture 2. To assess the detonation length-scale effects on the detonation diffracting through an obstacle, we simulate the detonation propagating along the semicircular obstacle with $r/l_i = 25$ and $l_i = 1.254$ mm. The results of transverse detonation are plotted in Fig. 17. A pair of transverse detonations induced by a local explosion propagate upward and downward, respectively, and they sweep along the shocked but unreacted mixtures [32]. This is different from the results in Fig. 9, which shows that there is only one single transverse detonation for mixture 1.

To demonstrate the process of transverse detonation formation, in Fig. 18 we plot the evolution of density gradient contours. Two weak triple points T1 and T2 propagate downwardly and upwardly along the diffracted wave, respectively. The pressure waves P1 and P2 are induced by the decoupled

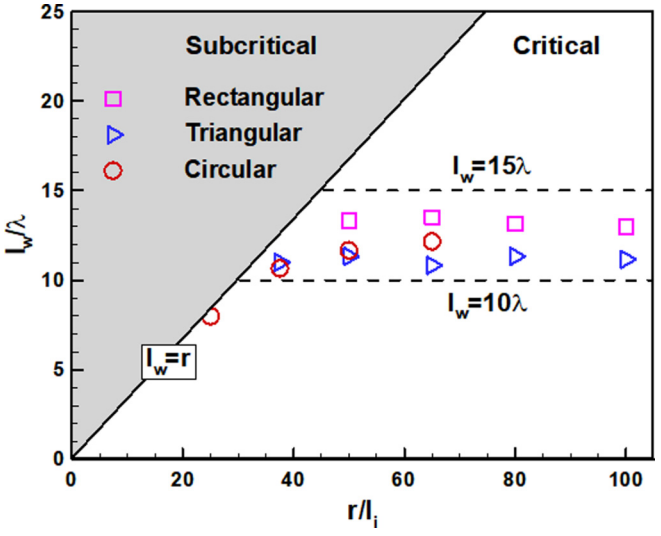

FIG. 16. Change of the normalized wall reflection distance from the obstacle apex to the reflection point of transverse detonation, l_w/λ, with normalized obstacle size, r/l_i, for different obstacle shapes.

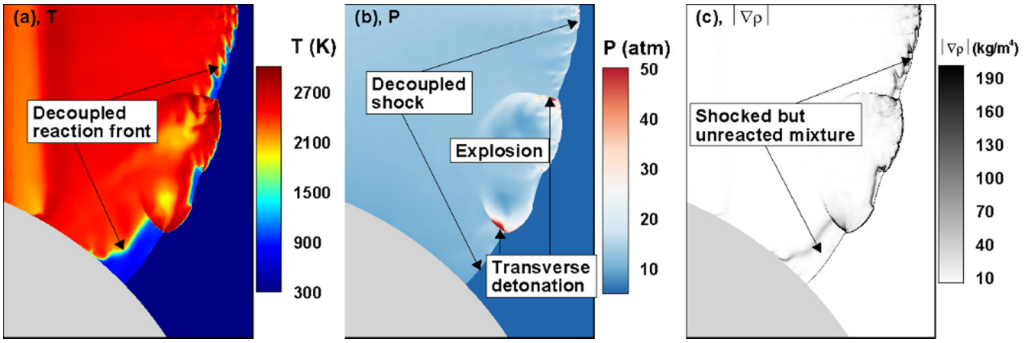

FIG. 17. Temperature, pressure, and density gradient contours of transverse detonation formation in mixture 2 for a semicircular obstacle with $r/l_i = 25$ and $l_i = 1.254$ mm.

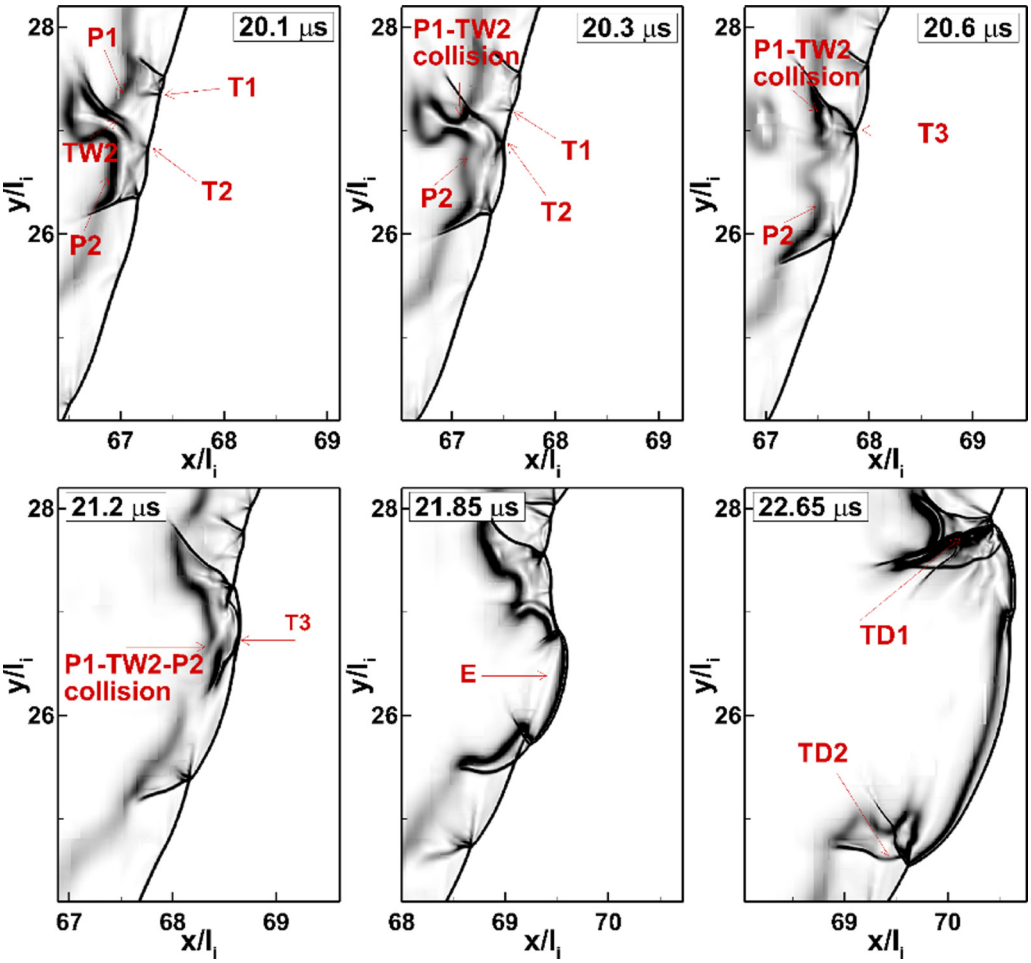

FIG. 18. Evolution of density gradient contours for a semicircular obstacle with $r/l_i = 25$ and $l_i = 1.254$ mm. $T1$–$T3$ represent triple points, $TW2$ represents transverse wave of $T2$, $P1$ and $P2$ represent pressure waves, E represents local explosion, and $TD1$ and $TD2$ represent transverse detonations.

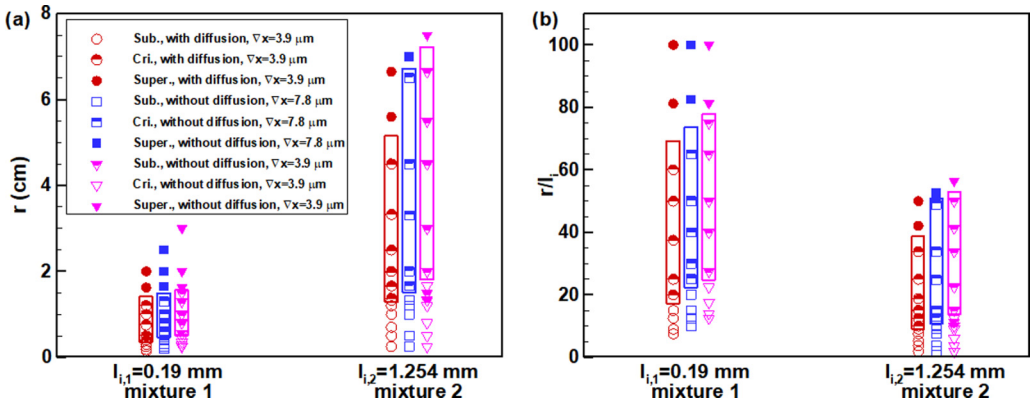

FIG. 19. Distributions of three regimes for mixtures 1 and 2 with induction lengths $l_{i,1}$ and $l_{i,2}$, respectively. Different meshes with and without diffusion term are considered. (a) No normalization, (b) with normalization by induction length.

reaction front. At $t = 20.3\,\mu$s, the transverse wave TW2 of triple point T2 propagates upward and collides with the pressure wave P1, resulting in the formation of new shock wave P1-TW2. At $t = 20.6\,\mu$s, the collision of two triple points T1 and T2 generates the new triple point T3. At $t = 21.2\,\mu$s, the pressure wave P2 further collides with the shock wave P1-TW2 and forms strong shock wave P1-TW2-P2 near the triple point T3. Thereafter, a local explosion, E, resulting from the strong shock wave is observed at $t = 21.85\,\mu$s, and two transverse detonations TD1 and TD2 develop at $t = 22.65\,\mu$s. In summary, the fold and collision of shock waves are crucial for transverse detonation formation [2,15].

The distributions of three regimes are observed for a semicircular obstacle in mixture 1. Similarly, we calculate detonation diffracting along a semicircular obstacle with different radii in mixture 2. To assess the effects of numerical and physical diffusions on regime distributions, the simulations with and without diffusion terms at different mesh levels are conducted and the results for mixtures 1 and 2 are compared in Fig. 19. It is found that the critical obstacle radius of transverse detonation formation is larger for mixture 2 with longer induction length. Note that in multidimensional cellular detonation, the transverse wave spacing is defined as the vertical distance when the reflection of transverse waves with each other occurs, and it is proportional to the induction length [33,34]. Therefore, for mixture 2 with longer induction length, the transverse wave spacing is larger. For a fixed obstacle radius, the transverse wave spacing is relatively large compared to the obstacle radius for mixture 2 and thus the critical obstacle radius of transverse detonation formation becomes larger. To eliminate the influence of detonation characteristic length, in Fig. 19(b) the obstacle radius for two mixtures is normalized by the corresponding induction length of the mixture. Figure 19(b) shows that the normalized critical obstacle radii become closer. This indicates that the formation of transverse detonation is nearly independent of nitrogen dilution for weakly unstable mixtures. In addition, the results for different meshes with and without diffusion term are qualitatively consistent. Only minor differences can be observed. For example, the comparison between the circle and triangle symbols indicate that the addition of the diffusion term makes the range of the critical regime smaller. In contrast, the slightly larger critical obstacle radius for transverse detonation formation is observed at a smaller mesh size. Therefore, both the physical and numerical diffusions facilitate the formation of transverse detonation and decrease the value of the critical regime.

IV. CONCLUSIONS

Two-dimensional simulations considering detailed chemistry and transport have been conducted for detonation diffracting through an obstacle. Different obstacle sizes and shapes are considered

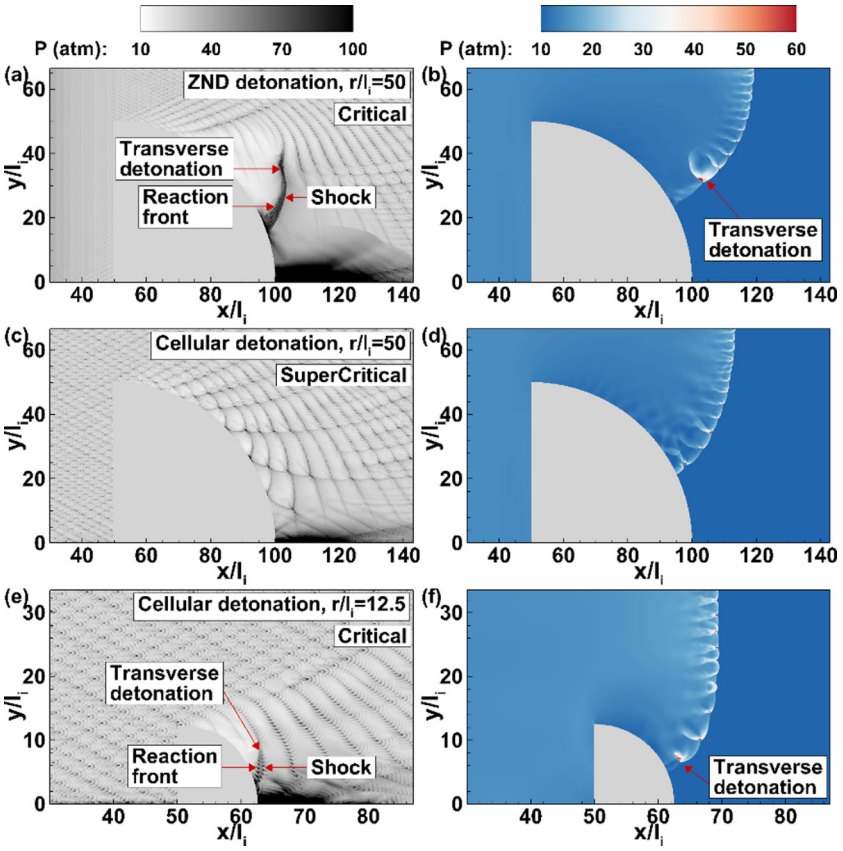

FIG. 20. Numerical soot foils (a), (c), (e) and pressure contours (b), (d), (f) for ZND (a), (b) and cellular (c), (d), (e), (f) detonations diffracting through a semicircular obstacle with different obstacle radii.

and their effects on the detonation diffraction process are assessed. For a semicircular obstacle, three regimes, subcritical, critical, and supercritical, are identified by increasing the radius of the obstacle. The competition between the energy release rate and expansion rate is used to explain the regime distribution. For a semicircular obstacle with larger radius and thereby smaller curvature, the expansion rate is relatively lower during the diffraction process and it is dominated over by the energy release rate. Therefore, a supercritical regime without detonation quenching is observed. The opposite holds for a semicircular obstacle with smaller radius. For triangular and rectangular obstacles, there is no supercritical regime even at large obstacle size.

The critical regime with the formation of transverse detonation is investigated in detail. It is found that the critical obstacle size for transverse detonation formation is the smallest for a semicircular obstacle but the largest for a rectangular obstacle. Unlike the critical obstacle size, the wall reflection distance of transverse detonation is always in the range of 10–15 times the detonation cell width and independent of the obstacle size and shape. Furthermore, the characteristics of transverse detonation are studied for two types of mixtures, hydrogen/air without and with nitrogen dilution. It is found that the larger obstacle size is required for transverse detonation formation in hydrogen/air with nitrogen dilution. This is because nitrogen dilution can increase detonation induction length and transverse wave spacing. After normalization by corresponding detonation induction length, the critical obstacle size for transverse detonation formation is close. This indicates that the formation of transverse detonation is nearly independent of nitrogen dilution.

TABLE IV. Four types of mesh considering different base mesh sizes and levels.

Mesh	Mesh 1	Mesh 2	Mesh 3	Mesh 4
Base mesh size (μm)	250	250	250	125
Mesh level	Five levels	Six levels	Seven levels	Six levels
Finest mesh size (μm)	7.8	3.9	1.95	1.95

It is noted that only weakly unstable mixtures are considered here. Lee [35] has proposed that detonation diffraction behavior involving shock-reaction decoupling, local explosion, and detonation reinitiation is significantly different in weakly and highly unstable mixtures. Therefore, the simulations for detonation diffraction in highly unstable mixtures deserve further study and the differences of the detonation reinitiation mechanism in weakly and highly unstable mixtures will be illustrated.

ACKNOWLEDGMENTS

This work was supported by the National Natural Science Foundation of China (Grant No. 51861135309), and China Postdoctoral Science Foundation (Grant No. 2020M680460). The simulations were conducted on the High Performance Computing Platform of the Center for Life Science at PKU and on the Tianhe-2A supercomputer in Guangzhou, China. We thank Prof. Ralf Deiterding at University of Southampton for his help on using AMROC.

APPENDIX A: ZND AND CELLULAR DETONATION INITIATION

Figure 20 shows that for $r/l_i = 50$, leading shock decouples with the reaction front as ZND detonation diffracts through an obstacle and then local explosion occurs following the formation

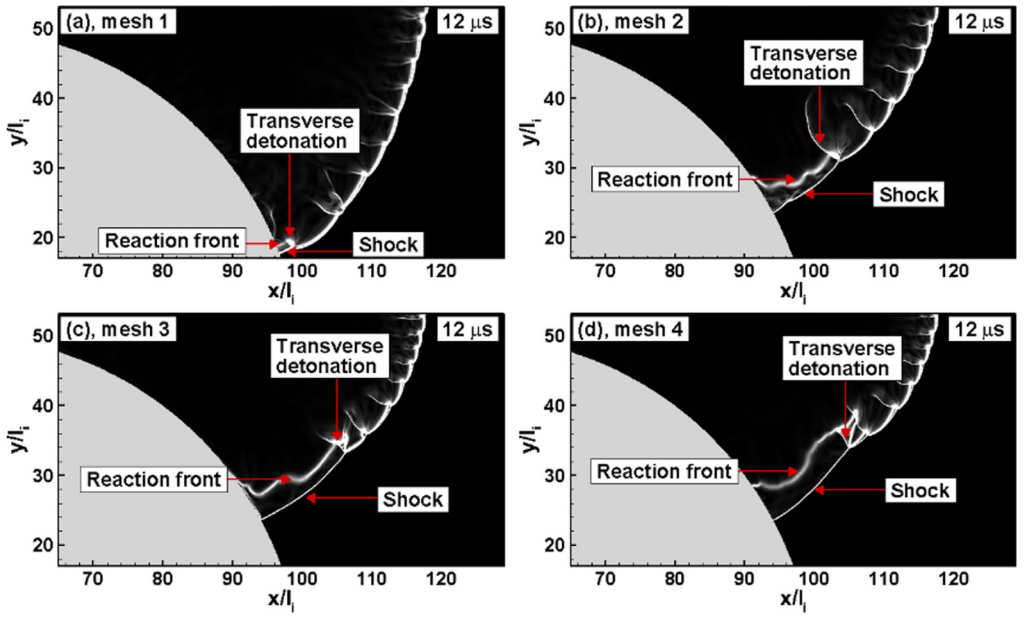

FIG. 21. The distributions of the density gradient contours for four types of mesh. The semicircular obstacle with $r/l_i = 50$ (i.e., critical regime) was used.

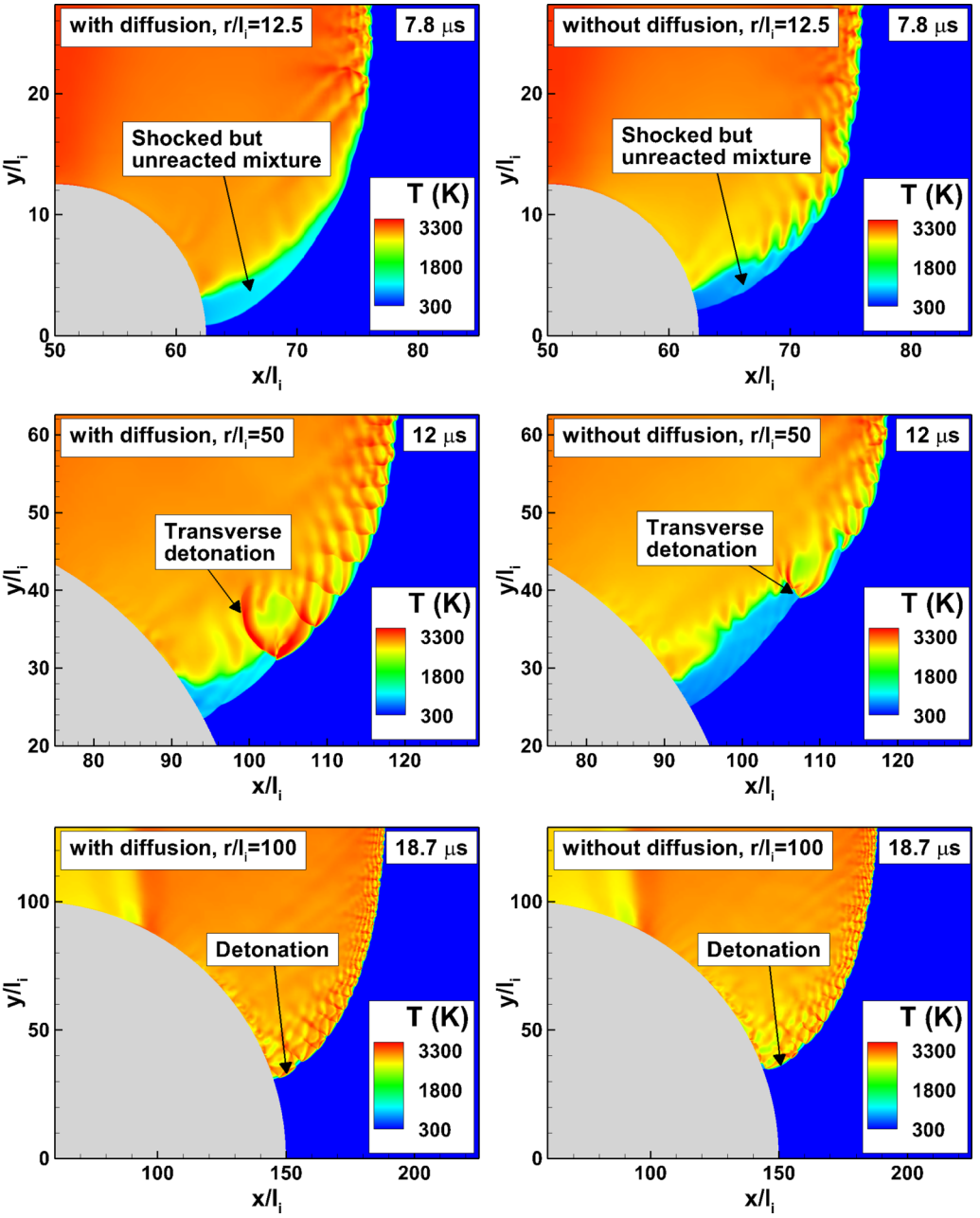

FIG. 22. Temperature contours for detonation diffracting through a semicircular obstacle with diffusion terms (left column) and without diffusion terms (right column). Different obstacle radii of $r/l_i = 12.5$ (top row), 50 (middle row), and 100 (bottom row) are considered.

of transverse detonation. However, when the cellular detonation with a fully developed intrinsic cellular structure diffracts the obstacle, there is no shock-reaction decoupling for $r/l_i = 50$. As the obstacle radius is decreased to $r/l_i = 12.5$, similar phenomena of shock-reaction front decoupling and the following formation of transverse detonation are observed for cellular detonation initiation.

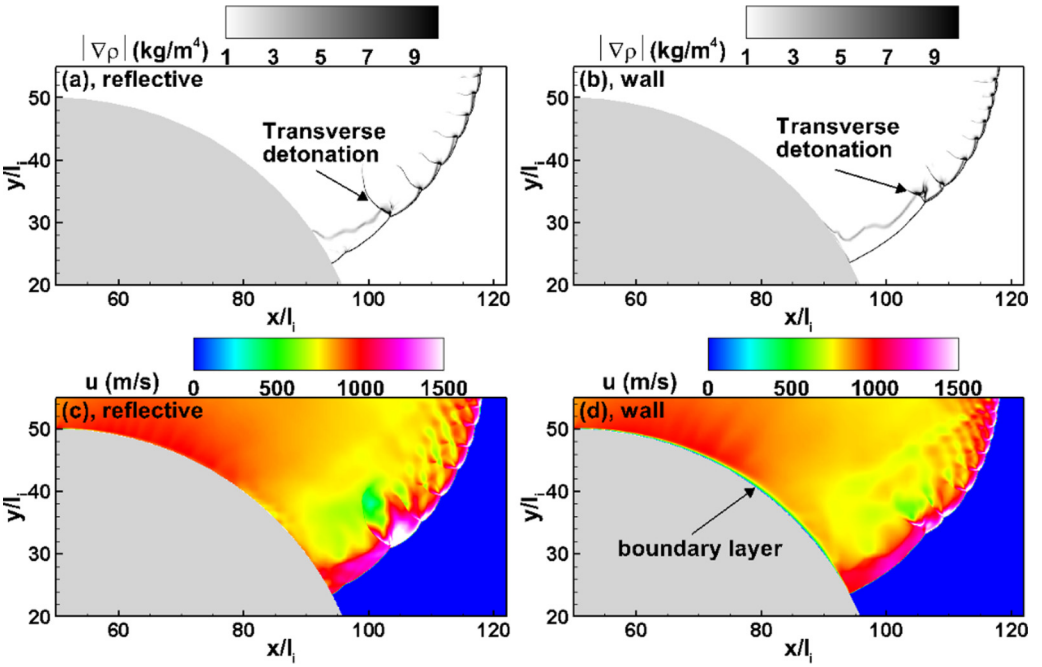

FIG. 23. (a), (b) Density gradient contour considering reflective and wall boundary condition on an obstacle surface, respectively; (c), (d) flow speed contour considering reflective and wall boundary condition on obstacle surface, respectively, for detonation propagating through a semicircular obstacle with $r/l_i = 50$.

Therefore, as detonation diffracts through the obstacle, the critical obstacle radius of transverse detonation formation for cellular detonation initiation is smaller than that for ZND detonation. This indicates that the cellular instability can promote the reinitiation process in a stoichiometric H_2/air mixture. The cellular instabilities result in the interaction of the transverse shock waves [30,31]. The collisions between the transverse shock waves induce local explosions and follow the formation of transverse detonation, which indicates the detonation reinitiation.

APPENDIX B: SIMULATIONS FOR FOUR TYPES OF MESH

Figure 21 plots distributions of density gradient contours for detonation diffracting through a semicircular obstacle with $r/l_i = 50$. Four types of mesh were considered, shown in Table IV. Figure 21 shows that the critical regimes with formation of transverse detonation are still observed and the detonation propagation speeds are the same for the four types of mesh. The location of transverse detonation for mesh 2 is nearly the same as that for meshes 3 and 4, which differs from that for mesh 1. Therefore, mesh 2 with the finest mesh size of 3.9 μm is used in the present simulations. Moreover, the effects of mesh size on the range of the critical regime with transverse detonation formation have been discussed in Fig. 19 and the results indicate that only minor differences can be observed for detonation propagating across an obstacle for different mesh sizes.

APPENDIX C: EFFECTS OF DIFFUSION TERMS

The simulations for detonation diffracting through an obstacle with and without diffusion terms were conducted and the results are shown in Fig. 22. It is seen that the regime distributions are the same for detonation diffracting through a semicircular obstacle with and without diffusion

terms, although some minor differences are observed. Specifically, for $r/l_i = 12.5$, reaction fronts behind the leading shock are more wrinkled for simulation without diffusion terms. As the obstacle radius increases to $r/l_i = 50$, the transverse detonation occurs earlier for simulation with diffusion terms. Wioth a further increase of obstacle radius to $r/l_i = 100$, the results are nearly the same in simulations both with and without diffusion terms. Moreover, the effects of the diffusion term on the range of the critical regime with transverse detonation formation have been investigated and shown in Fig. 19. The results indicate that there is a slight difference in the critical regime. Addition of the diffusion term promotes the formation of transverse detonation and makes the critical obstacle radius smaller.

APPENDIX D: EFFECTS OF BOUNDARY CONDITION OF OBSTACLE SURFACE

The simulations considering both wall and reflective boundary conditions on an obstacle surface were conducted and the results were plotted in Fig. 23. It is found that the wall boundary layer slightly affects the shape of the transverse wave. However, the regime distributions of detonation diffraction are the same for simulations considering both wall and reflective boundary conditions on an obstacle surface, respectively.

[1] V. V. Mitrofanov and R. I. Soloukhin, The diffraction of multifront detonation waves, Sov. Phys. Dokl. **9**, 1055 (1965).

[2] D. H. Edwards, G. O. Thomas, and M. A. Nettleton, The diffraction of a planar detonation wave at an abrupt area change, J. Fluid Mech. **95**, 79 (1979).

[3] B. Khasainov, H.-N. Presles, D. Desbordes, P. Demontis, and P. Vidal, Detonation diffraction from circular tubes to cones, Shock Waves **14**, 187 (2005).

[4] S. B. Murray and J. H. S. Lee, On the transformation of planar detonation to cylindrical detonation, Combust. Flame **52**, 269 (1983).

[5] X. Q. Yuan, X. C. Mi, H. D. Ng, and J. Zhou, A model for the trajectory of the transverse detonation resulting from re-initiation of a diffracted detonation, Shock Waves **30**, 13 (2019).

[6] F. Bartlmä and K. Schröder, The diffraction of a plane detonation wave at a convex corner, Combust. Flame **66**, 237 (1986).

[7] S. Gallier, F. Le Palud, F. Pintgen, R. Mével, and J. E. Shepherd, Detonation wave diffraction in H_2-O_2-Ar mixtures, Proc. Combust. Inst. **36**, 2781 (2017).

[8] X. Yuan, J. Zhou, Z. Lin, and X. Cai, Numerical study of detonation diffraction through 90-degree curved channels to expansion area, Int. J. Hydrogen Energy **42**, 7045 (2017).

[9] A. Kawasaki and J. Kasahara, A novel characteristic length of detonation relevant to supercritical diffraction, Shock Waves **30**, 1 (2019).

[10] Y. Nagura, J. Kasahara, Y. Sugiyama, and A. Matsuo, Comprehensive visualization of detonation-diffraction structures and sizes in unstable and stable mixtures, Proc. Combust. Inst. **34**, 1949 (2013).

[11] Y. Nagura, J. Kasahara, and A. Matsuo, Multi-frame visualization for detonation wave diffraction, Shock Waves **26**, 645 (2016).

[12] G. B. Whitham, A new approach to problems of shock dynamics. Part. I. Two-dimensional problems, J. Fluid Mech. **2**, 145 (1957).

[13] F. Pintgen and J. E. Shepherd, Detonation diffraction in gases, Combust. Flame **156**, 665 (2009).

[14] R. I. Soloukhin and K. W. Ragland, Ignition processes in expanding detonations, Combust. Flame **13**, 295 (1969).

[15] M. Arienti and J. E. Shepherd, A numerical study of detonation diffraction, J. Fluid Mech. **529**, 117 (2005).

[16] S. B. Murray and J. H. S. Lee, The influence of physical boundaries on gaseous detonation waves, Prog. Astronaut. Aeronaut. **106**, 329 (1986).

[17] E. Schultz, Detonation diffraction through an abrupt area expansion, Ph.D. thesis, California Institute of Technology, 2000.
[18] R. Deiterding, A parallel adaptive method for simulating shock-induced combustion with detailed chemical kinetics in complex domains, Comput. Struct. **87**, 769 (2009).
[19] J. Li, Z. Zhao, A. Kazakov, and F. L. Dryer, An updated comprehensive kinetics model of hydrogen combustion, Int. J. Chem. Kinet. **36**, 566 (2004).
[20] Y. Wang, W. Han, R. Deiterding, and Z. Chen, Effects of disturbance on detonation initiation in $H_2/O_2/N_2$ mixture, Phys. Rev. Fluids **3**, 123201 (2018).
[21] Y. Wang, C. Huang, R. Deiterding, H. Chen, and Z. Chen, Propagation of gaseous detonation across inert layers, Proc. Combust. Inst. **38**, 3555 (2021).
[22] R. Deiterding, High-resolution numerical simulation and analysis of Mach reflection structures in detonation waves in low-pressure H_2-O_2-Ar mixtures: A summary of results obtained with the adaptive mesh refinement framework AMROC, J. Combust. **2011**, 1 (2011).
[23] X. Cai, J. Liang, R. Deiterding, Y. Mahmoudi, and M. Sun, Experimental and numerical investigations on propagating modes of detonations: Detonation wave/boundary layer interaction, Combust. Flame **190**, 201 (2018).
[24] X. Cai, R. Deiterding, J. Liang, M. Sun, and D. Dong, Dynamic detonation stabilization in supersonic expanding channels, Phys. Rev. Fluids **4**, 083201 (2019).
[25] R. R. Bhattacharjee, Experimental investigation of detonation re-initiation mechanisms following a Mach reflection of a quenched detonation, M.A.Sc. thesis, University of Ottawa, 2013.
[26] S. S. Lau-Chapdelaine, Numerical simulations of detonation re-initiation behind an obstacle, M.A.Sc. thesis, University of Ottawa, 2013.
[27] I. O. Moen, S. B. Murray, D. Bjerketvedt, A. Rinnan, R. Knystautas, and J. H. S. Lee, Diffraction of detonation from tubes into a large fuel-air explosive cloud, Proc. Combust. Inst. **19**, 635 (1982).
[28] J. Li, J. Ning, and J. H. S. Lee, Mach reflection of a ZND detonation wave, Shock Waves **25**, 293 (2015).
[29] A. V. Fedorov, T. A. Khmel, and Y. V. Kratova, Cellular detonation diffraction in gas-particle mixtures, Shock Waves **20**, 509 (2010).
[30] M. I. Radulescu, G. J. Sharpe, and C. K. Law, Effect of cellular instabilities on the blast initiation of weakly unstable detonations, in *Proceedings of the 21st International Colloquium on the Dynamics of Explosions and Reactive Systems* (Poitiers, France, 2007).
[31] H. D. Ng, C. B. Kiyanda, G. H. Morgan, and N. Nikiforakis, The influence of high-frequency instabilities on the direct initiation of two-dimensional gaseous detonations, in *Proceedings of the 25th International Colloquium on the Dynamics of Explosions and Reactive Systems* (Leeds, UK, 2015).
[32] L. Shi, K. C. K. Uy, and C. Y. Wen, The re-initiation mechanism of detonation diffraction in a weakly unstable gaseous mixture, J. Fluid Mech. **895**, A24 (2020).
[33] S. Boulal, P. Vidal, and R. Zitoun, Experimental investigation of detonation quenching in non-uniform compositions, Combust. Flame **172**, 222 (2016).
[34] J. H. S. Lee, *The Detonation Phenomenon* (Cambridge University Press, Cambridge, 2008).
[35] J. H. S. Lee, in *Dynamics of Exothermicity*, edited by J. Bowen (Gordon and Breach, Amsterdam, 1996), pp. 321–336.